Separating Attoliter-Sized Compartments Using Fluid Pore-Spanning Lipid Bilayers

Thomas D. Lazzara,[†] Christian Carnarius,[†] Marta Kocun,[‡] Andreas Janshoff,[‡] and Claudia Steinem[†,*]

[†]Institute of Organic and Biomolecular Chemistry, Tammannstrasse 2, 37077 Göttingen, Germany, and [‡]Institute of Physical Chemistry, Tammannstrasse 6, 37077 Göttingen, Germany

ABSTRACT Anodic aluminum oxide (AAO) is a porous material having aligned cylindrical compartments with 55−60 nm diameter pores, and being several micrometers deep. A protocol was developed to generate pore-spanning fluid lipid bilayers separating the attoliter-sized compartments of the nanoporous material from the bulk solution, while preserving the optical transparency of the AAO. The AAO was selectively functionalized by silane chemistry to spread giant unilamellar vesicles (GUVs) resulting in large continuous membrane patches covering the pores. Formation of fluid single lipid bilayers through GUV rupture could be readily observed by fluorescence microscopy and further supported by conservation of membrane surface area, before and after GUV rupture. Fluorescence recovery after photobleaching gave low immobile fractions (5−15%) and lipid diffusion coefficients similar to those found for bilayers on silica. The entrapment of molecules within the porous underlying cylindrical compartments, as well as the exclusion of macromolecules from the nanopores, demonstrate the barrier function of the pore-spanning membranes and could be investigated in three-dimensions using confocal laser scanning fluorescence imaging.

KEYWORDS: anodic aluminum oxide · fluorescence microscopy · fluorescence recovery after photobleaching · molecular encapsulation · nanoporous substrates · silane chemistry

The modification of solid surfaces with lipid monolayers and bilayers, obtained from the spreading of vesicles, requires careful attention to surface geometry and to surface chemistry.[1,2] Functionalization strategies are designed to specifically interact with either the hydrophilic phospholipid head-groups or with the hydrophobic lipid tails in order to form different solid-supported membrane architectures.[1,3] A prominent example are hybrid lipid membranes,[4,5] where the lower mobile lipid leaflet is replaced with an immobile hydrophobic self-assembled monolayer. To decouple the membrane from the solid support and increase the mobility of the lipids, polymer-cushioned bilayers[6−8] or tethered lipid bilayers[9,10] have been developed. Fluid bilayer membranes,[2,11−15] where a thin water cushion separates the bilayer from the support,[14,16,17] are typically formed on hydrophilic substrates such as SiO_2[18−20] and other hydroxyl-terminated surfaces, such as oxygen-plasma-treated siloxane films[21,22] and mixed self-assembled monolayers containing carboxylic acids.[23−27]

In recent years, as an improvement over solid-supported membranes (SSMs), pore-spanning lipid membranes formed on porous substrates have been introduced to probe the physical properties of lipid membranes and the functionality of different transmembrane proteins.[28−31] Pore-spanning fluid membranes[32−34] are particularly attractive since they combine the mechanical stability of SSMs and the advantage of free-standing lipid membranes providing two accessible aqueous compartments. Melosh and co-workers have recently shown the long-term stability and sealing capability of pore-spanning membranes formed over 100−1000 nm pores[35] by the bubble collapse technique on Al_2O_3 and SiO_2.[36,37] Many preparations rely on gold−thiol chemistry to functionalize the porous interface with alkanethiols, fluorinated alkanethiols, or phospholipid and cholesterol derivatives in order to form hybrid pore-spanning membranes.[30,38−40] These membranes are hybrid on the pore-rim surface, that is, composed of a covalently anchored self-assembled monolayer and a fluid lipid leaflet atop, while remaining homogeneous bilayers in the porous areas. Hybrid pore-spanning membranes have the advantage of being easily prepared on porous substrates, but are considerably prestressed because of the hydrophobic nature of the pore-rim tethering.[41] By using hydrophilic porous surfaces obtained through the deposition of SiO_2 directly onto a gold surface,[32] or directly using porous SiO_2 obtained by lithographical means,[42−44] fluid pore-spanning bilayers have been achieved. For generating pore-spanning membranes following preparation protocols that are based on vesicle spreading, the surface must be sufficiently

* Address correspondence to csteine@gwdg.de.

Received for review April 6, 2011 and accepted July 28, 2011.

Published online July 28, 2011
10.1021/nn201266e

reactive so that it induces liposome rupture by vesicle-deformation in response to strong adhesion, while simultaneously avoiding the rupture of the pore-spanning part.[42,45] Furthermore, an often understated challenge is to avoid lining of the pore-interior walls with lipids,[42,46−48] which can be achieved by having a pore-interior surface chemistry that is distinct from the pore-rim surface chemistry.

For producing pore-spanning membranes, pore arrays are prepared preferentially in silicon by photolithography.[40,42−44,49] Anodic aluminum oxide (AAO) is of particular interest because cylindrical nonintersecting pores with defined pore diameters of $d_0 < 100$ nm are easily achieved by anodization without the use of photolithography. Another advantage is its optical transparency[50−52] when prepared with structural features below 100 nm, which allows for fluorescence microscopy detection of fluorescent molecules within the pores.[53,54] Optical transparency also implies that refractive index-based techniques can be used to study changes occurring within the nanopores.[52,55−57] However, for such studies, metals such as gold cannot be used as they quench fluorescence,[58] and significantly decrease light propagation in thin nanoporous dielectric films, even when trace amounts are incorporated within these.[59] Surface functionalizations that modify the material with reactive monolayers must be based on silanes or phosphonates, or alternatively inorganic oxides deposited by chemical vapor deposition or sputtering techniques.

In this study, we developed a method that allows nanoporous AAO substrates to be coated with a thin hydroxyl-terminated film at the interface between the nanoporous material and the bulk solution. We show that these functionalized AAO substrates allow rupturing of POPC GUVs forming pore-spanning bilayer patches with laterally mobile lipids. The optical transparency of the alumina substrate enabled us to visualize the entrapment of fluorescent molecules within the attoliter-sized compartments by confocal laser scanning microscopy. We expect this setup to provide a realistic mimic of the plasma membrane−cytoskeleton framework that allows the incorporation of functional transmembrane proteins and which will enable us to establish addressable and tunable (electro)-chemical gradients across the membranes.

RESULTS AND DISCUSSION

Pore-Spanning Lipid Membranes on Functionalized AAO. We used AAO substrates with an interpore distance of p = 100 nm, and pore diameters that were enlarged to d_0 = 55−60 nm (Figure 1A, top). The AAO thickness was adjusted to h = 3.5 or 7 μm (Figure 1A, bottom). To produce pore-spanning membranes by phosphocholine lipid vesicle spreading on AAO substrates (Figure 1B), vesicles have to adhere strongly onto the surface and

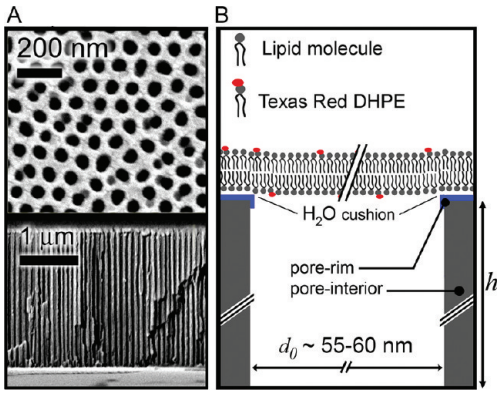

Figure 1. (A) Scanning electron microscopy images of an AAO substrate viewed from the top (top image) and the cross-section (bottom image). The AAO was mounted as a thin-film on a glass substrate. The layered structure, from top to bottom, in the cross section is AAO/Cr−Au/adhesive/glass (glass not visible). (B) Schematic view of a solvent-free fluid pore-spanning membrane covering an AAO nanopore.

then rupture to form a lipid bilayer that is located at the AAO/bulk interface. However, lipid vesicles adhere only weakly and do not rupture on untreated or plasma treated (oxygen or argon plasma) AAO surfaces (Supporting Information, Figure S1A) as expected from alumina substrates.[37]

This is due to the chemical nature of the AAO surface, which has contributions from both Al_2O_3 and surface incorporated oxalic acid anions.[60] Additionally, the porosity of the AAO substrate (25−30%) decreases the interfacial interaction area and therefore reduces the rupture propensity. Chemical surface functionalization of AAO is therefore required to generate a hydrophilic surface that induces liposome rupture, while simultaneously ensuring that the substrate remains optically transparent. To generate the required functionality on the AAO substrates, these were first silanized with mercaptopropyl-triethoxysilane by gas phase reaction, followed by treatment with a temporary thin gold layer (10−20 nm), thermally evaporated under vacuum. The gold layer served as a protective mask that prevented the removal of the pore-rim surface functionalization as reported previously.[61] The sample was then treated with O_2 plasma for 60 s, followed by Ar plasma for 60 s, which removed the organosilane functionalization from the nonprotected pore-interior surface by both reactive oxygen radicals and physical ablation,[62,63] while the gold-coated pore-rim surface functionalization remained intact. Afterward, the gold layer was removed by I_2/KI. The substrate was then rinsed, dried, and treated with O_2 plasma for about 15−30 s to oxidize the ethoxy- and mercaptopropyl groups on the pore-rim surface without ablation. The substrates were incubated with fluorescently labeled (1 mol % Texas Red DHPE) giant unilamellar vesicles (GUVs) composed of POPC to investigate whether vesicles spread on such surface and to form pore-spanning membranes. GUVs have

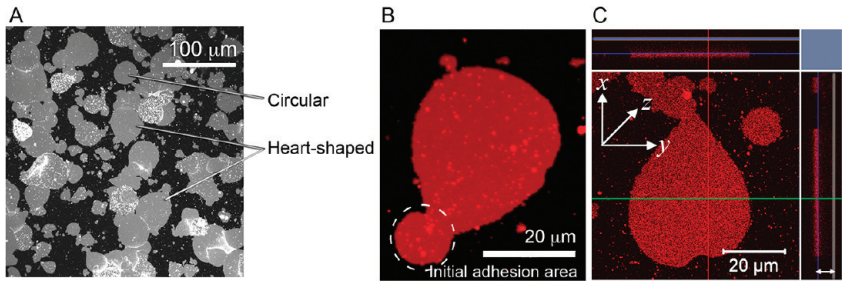

Figure 2. (A) Pore-spanning lipid bilayer patches obtained from the rupture of giant unilamellar POPC vesicles doped with 1 mol % Texas Red DHPE on functionalized AAO substrates. (B) Enlarged view of a heart-shaped lipid membrane patch, formed by vesicle rupture. The initial contact area of the sessile GUV prior to spreading is denoted by a dotted white line. (C) Confocal *z*-stack image illustrating the formation of a pore-spanning membrane atop functionalized AAO (d_0 = 60 nm, h = 3.5 μm). The double-headed arrow shows the AAO thickness, and the thick blue line marks the pore bottoms. Scale bar also applies to the *z*-direction profiles.

the advantage that they are relatively easy to image by optical microscopy and, upon rupturing, form large continuous membrane patches with an area of several tens of square micrometers. POPC GUVs filled with 0.3 M sucrose sedimented onto the functionalized AAO, because the outer solution was composed of lower density PBS buffer.

The process of vesicle attachment and spreading was followed by video microscopy. Typically, a GUV approached the AAO surface, then firmly attached and ruptured. The rupture step occurred within one video frame (30 frames s^{-1}) and thus could not be resolved in more detail with our camera (Supporting Information, Movie S1).

Figure 2A shows the result of the spreading of fluorescently labeled GUVs on the functionalized porous AAO substrate. We observed two principle shapes of the planar pore-spanning membrane patches. While round and symmetric patches occur, predominantly asymmetric heart-shaped patches were observed. The shape is a result of the rupture initiation site that is either at the top (round patch) of the adsorbed vesicle or closer to its side (heart-shaped patch), as reported by Hamai *et al.*[13] In Figure 2B, a typical noncircular patch formed after rupture near the vesicle's side is shown, varying slightly from a heart-shape. The initial circular AAO adhesion area with the POPC GUV is also shown, and the deformation-induced rupture at the liposome side leads to vesicle spreading away from the adhesion area. Owing to the AAO transparency, *z*-stacks taken with confocal laser scanning fluorescence microscopy (CLSM) allowed us to show that pore-spanning membranes were formed, in contrast to membranes lining the pore-interior. The confocal *z*-stack image shown in Figure 2C demonstrates that the fluorescence is only localized atop the AAO substrate (h = 3.5 μm), indicating that the membranes were exclusively pore-spanning.

We next asked the question, whether the planar membranes are continuous single bilayers and whether they experience an area expansion after adhesion and spreading, that is, whether they are prestressed, a phenomenon that was observed on hybrid pore-spanning membranes attached to hydrophobically functionalized pore rims.[41] Area expansion for hybrid systems occurs due to the excess lipids being displaced by the immobile hydrophobic functionalization of the pore rims. For fluid non-tethering hydrophilic pore rims, area conservation is expected since the bilayer structure of the GUV is directly reproduced on the porous surface. The area of a pore-spanning membrane patch, as observed in fluorescence imaging, was compared to the value expected from the calculated area of a GUV before its rupture. Figure 3A shows a fluorescence image of a POPC GUV before and after rupture. An outline delimiting the size of the final membrane patch is drawn in white on both images. The equatorial contour of the GUV prior to rupture is perfectly circular (left image of Figure 3A). A fluorescent area is observed after rupture (right image of Figure 3A). For this particular GUV, we found that the surface area after rupture, calculated by pixel analysis, was 93 μm^2 and agreed with the predicted GUV surface area, estimated from the diameter of the GUV, which was 103 μm^2. Lipid membrane surface area was conserved in agreement with the formation of a fluid bilayer. The error associated with the lipid membrane area, for recorded rupture events by confocal fluorescence, was about 10% between estimated and calculated areas (n = 5). The error mainly arises from the uncertainty in the estimation of the vesicle diameter prior to rupture.

To further confirm that continuous planar and fluid pore-spanning lipid bilayers are formed by this method, we performed fluorescence recovery after photobleaching (FRAP) experiments. POPC GUVs labeled with 0.1 mol % of Bodipy DHPE were used to form lipid bilayer patches on the functionalized AAO. Figure 3B shows a typical fluorescence recovery curve with a fit to the data, following the theory of Axelrod *et al.*[64] An average mobile fraction of 90 $\pm$ 5%, and a diffusion coefficient of 3.8 $\pm$ 0.8 $\mu m^2\ s^{-1}$ (n = 6) were obtained for POPC bilayers. The small immobile fraction indicates that both the top and bottom leaflet of the bilayer are mobile.[1,65] It has been reported that the diffusion

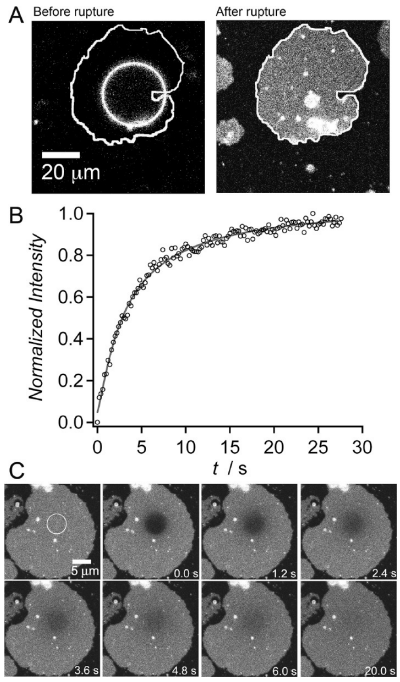

Figure 3. (A) CLSM image taken at approximately the center focal plane of a POPC GUV right before its adsorption and rupture on hydrophilic AAO. Lipid membrane area after rupture (93 μm^2) is preserved in comparison to the area of the vesicle (103 μm^2) before rupture, which agrees with the vesicle rupture mechanism leading to fluid lipid bilayers with continuous double-leaflet structure. Outline of the bilayer patch after spreading is shown in white on both images. (B) Recovery curve of a FRAP experiment performed on a membrane patch obtained from Bodipy DHPE (0.1 mol %) labeled POPC GUVs. For this curve, the diffusion coefficient obtained was 4 $\pm$ 1 $\mu m^2\ s^{-1}$, with an immobile fraction of 5%. (C) Time-elapsed images of a typical FRAP experiment showing uniform fluorescence recovery after photobleaching.

coefficients of lipids vary with the nature of the underlying supporting substrate; for alumina surfaces D_{lipids} = 0.6 $\mu m^2\ s^{-1}$ was obtained,[36] while this value is greater on SiO_2 surfaces (D_{lipids} = 1−3 $\mu m^2\ s^{-1}$)[25,36,66] and even greater for giant vesicles (D_{lipids} = 7−8 $\mu m^2\ s^{-1}$).[66] The diffusion coefficient we obtained for the POPC bilayer patches is slightly larger than reported values for silica surfaces. It is important to realize that the limited lipid reservoir of these patches decreases the accuracy of the FRAP analysis in determining the diffusion constant and probably produces the apparent immobile fraction. The values obtained are therefore estimates, but nevertheless remain reasonably within the expected range for planar supported bilayers. Considering that the pore-spanning part of the deposited bilayers most likely displays a larger diffusion constant (>4−5 $\mu m^2\ s^{-1}$) in comparison to the lipids in close vicinity to the surface (<3 $\mu m^2\ s^{-1}$), the average diffusion constant is expected to be in between both values.

Macromolecular Exclusion and Molecular Encapsulation by Pore-Spanning Membranes. GUVs of 5−25 μm in diameter rupture to form pore-spanning membranes that cover an area of 25−600 μm^2. These patches effectively separate thousands of individual attoliter-sized compartments (AAO nanopores) from the outer medium. Furthermore, the individually covered pores are isolated from each other because of the cylindrical geometry and because of the fact that the AAO pores are closed at the substrate bottom (see Figure 1A).

To prove the integrity of the lipid bilayer patches, we investigated whether the pore-spanning membranes exclude macromolecules from entering and adsorbing on the inner walls of the nanopores. Recently, we showed that avidin adsorbs quickly and irreversibly on the inner pore walls.[67] We used fluorescently labeled avidin (Alexa-488 avidin), which adsorbs electrostatically on the AAO porous surface (Supporting Information, Figure S2). Pore-spanning membranes composed of POPC and doped with Texas Red DHPE were first formed and Alexa-488 avidin was added afterward. Fluorescence images revealed that in the regions where pore-spanning membranes were formed, Alexa-488 fluorescence was absent. In contrast, the areas that were not covered by a membrane showed a bright green fluorescence because of protein adsorption on the inner pore walls (Figure 4A). Figure 4B schematically depicts the two possible protein adsorption scenarios: (i) with and (ii) without a pore-spanning membrane. In Figure 4C, two different focal plane views are shown, at the top AAO interface with the bulk solution where the lipid membrane is formed (top image) and within the AAO where no fluorescence was observed since neither lipids nor proteins were present within the PBS buffer filled AAO nanopores (bottom image). The *z*-projections clearly show that (1) the lipid fluorescence from the pore-spanning membrane is located at the top AAO surface only, (2) avidin can diffuse throughout the depth of the AAO substrate, and (3) fluorescently labeled proteins are excluded from entering the pores that are covered by a pore-spanning lipid bilayer.

Since the pore-spanning membranes served as a permeability barrier, we exploited their insulating nature to entrap small water-soluble molecules inside the pores, which do not adsorb onto the pore walls. Pore-spanning membranes were produced by spreading Texas Red DHPE doped POPC GUVs on the functionalized AAO surface in the presence of pyranine dye (10 mM) in PBS buffer. The sample was then rinsed with buffer to remove the pyranine from the solution. Fluorescence images (Figure 5A) demonstrate that in the regions where pore-spanning membranes were formed, pyranine molecules remained entrapped within the pores. These areas show persistence fluorescence after rinsing for more than 48 h. In areas where the membrane was not pore-spanning but still remained on the pore-rims, the Texas Red DHPE fluorescence was still visible, but the pyranine fluorescence was absent because the fluorophores were removed from the pores during rinsing. We also collected *z*-stacks, showing the

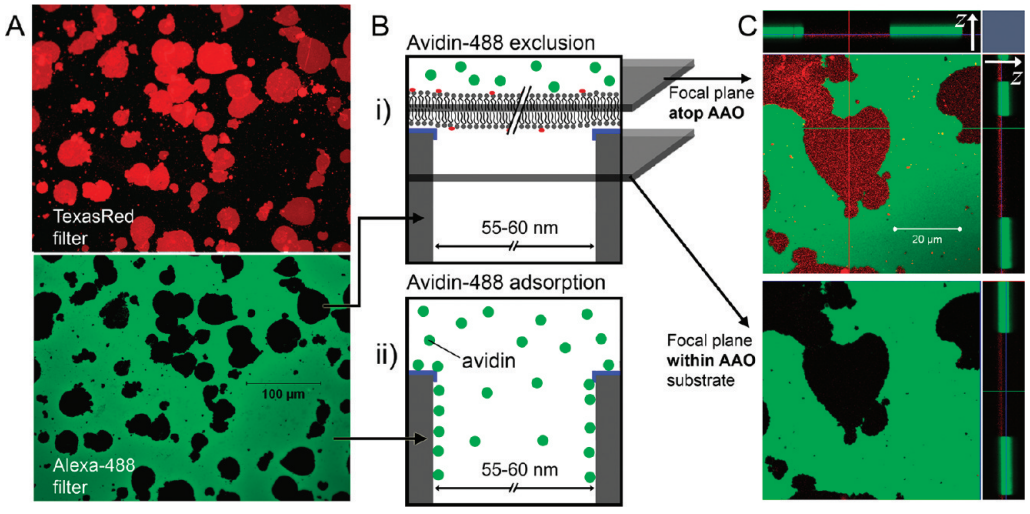

Figure 4. (A) CLSM images of AAO with POPC pore-spanning membranes (top image: TexasRed filter) that exclude Alexa-488 avidin (bottom image: Alexa-488 filter) from entering the pores. The protein is either excluded (dark) or adsorbed within unblocked nanopores (green). Pore-spanning membrane fluorescence correlates with the absence of protein fluorescence. (B) Schematic drawing of the two possible scenarios: (i) pore-spanning membrane blocks avidin entrance within pores and (ii) adsorption of avidin on uncovered pore rims. (C) Composite *z*-stack images (total *z*-distance: 15 μm) of a pore-spanning POPC bilayer preventing avidin entrance into the underlying pores (black areas). Top image: lipid membrane is located at the interface between the AAO and the bulk solution, showing both Texas Red DHPE and Alexa-488 avidin fluorescence in the overlay. Bottom image was taken within the center focal plane of the AAO film, where Texas Red DHPE fluorescence is no longer observed. Top and right side images are line profiles in the *z*-direction and clearly show that the membrane prevents the fluorescently labeled proteins from entering the pores.

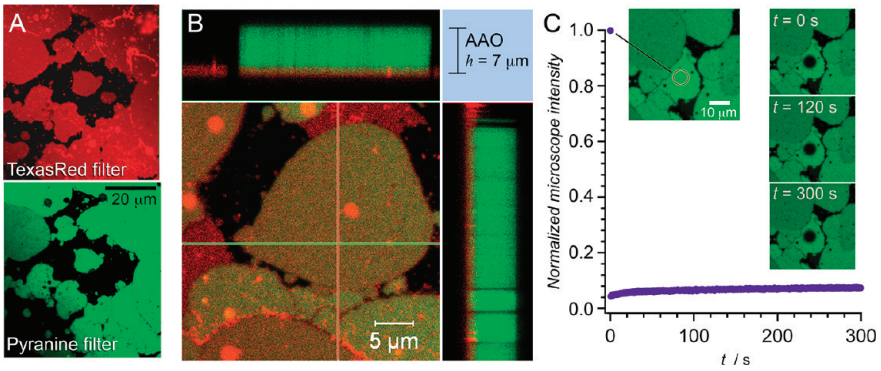

Figure 5. (A) 2D confocal fluorescence images of pore-spanning POPC lipid membranes with pyranine entrapped in the AAO pores. The green pyranine fluorescence (bottom, pyranine filter) correlates with the position of the POPC membranes (top, TexasRed filter). (B) 3D *z*-stack image of the membrane encapsulating dye molecules within the cylindrical nanopores of AAO (h = 7 μm). Only membrane-covered pores can entrap the pyranine dye. (C) Fluorescence recovery of the interior of the bleached nanoporous area filled with pyranine dye. Each nanopore is isolated from its neighbors and therefore, the fluorescence cannot recover. Inset shows the lack of fluorescence recovery at t = 0, 120, and 300 s (right).

fluorescence distribution in the vertical direction across these patches (Figure 5B). The localized fluorescence from the lipid membrane covering the top of the AAO interface can be observed, independently of the fluorescence from the encapsulated pyranine dye that fluoresces throughout the 7 μm thick AAO.

Since the cylindrical pores of AAO are not interconnected, each cylindrical pore is physically isolated from its neighbor. Therefore, the pyranine fluorescence in the photobleached area with encapsulated pyranine dye does not recover with time (Figure 5C, Supporting Information, Figure S3). In fact, fluorescence recovery was not observed within the bleached pores, even after 300 s, consistent with the assumption that the pyranine is localized in individually isolated pores. The small initial fluorescence recovery observed was due to unbleached dyes along the pore axis that diffused back into the focal plane. Interestingly, the pyranine fluorescence images also show that neighboring lipid membrane patches are discontinuous, showing interfacial faults between them. Each formed membrane patch corresponds to a single ruptured GUV and the dye does not remain entrapped in the pores lying at the interface between those patches.

This observation implies that the membranes in those regions are not pore-spanning. Membrane self-healing over those uncovered pores, at the interface between patches, is prevented by the underlying

porosity of the substrate. If a solvent-free pore-spanning membrane ruptures, its reformation is improbable since lipids tend to go around surface defects, rather than covering the pores.[68] This is in contrast to what has been observed for fluid SSMs, where defects are easily healed by lateral merger of membrane edges,[69] leading to uniform surface bilayer coverage. Although the surface lipid bilayer coverage of the AAO could be increased by adding a larger concentration of GUVs, a continuous bilayer over the entire AAO surface was not achieved because interfacial faults between patches remained observable throughout (Supporting Information, Figure S4 and S5). In fact, the fluorescence of a neighboring patch did not recover significantly when the latter was entirely photobleached, unlike in Figure 3, where rapid recovery within a patch is observed.

Impact of Surface Functionalization on Pore-Spanning Membrane Formation. We found that the intermediate gold-protective step, followed by O_2 and Ar plasma treatments, was essential for the vesicles to rupture and form pore-spanning membranes. If we applied only the O_2 plasma to silanized AAO samples, vesicles ruptured forming irregular patches. Confocal fluorescent *z*-stacks showed that these irregular domains had lipids that lined the inside of the nanopores, as well as having some areas where the lipid membranes remained pore-spanning (Supporting Information, Figure S1B). Fluorescently labeled Texas Red DHPE lipids were also located within the interior of the AAO porous film, rather than being localized only at the AAO top interface, which was in clear contrast to the pore-spanning lipid membrane patches shown in the fluorescence images of Figures 4 and 5. Ar plasma has been shown to modify surface films by physical ablation, while the reactive species present in O_2 plasma oxidize organic functional groups. By using both Ar and O_2 plasma and protecting the pore-rim surface with the temporary gold layer, we believe that the pore-interior silanization was sufficiently removed, such that the hydrophilic silanol groups were predominantly on the pore rims.

After removal of the protective gold layer, a short O_2 plasma treatment of 30 s was required to ensure that the organic functional groups on the pore-rim surface, that is, ethoxy and mercaptopropyl, were oxidized to silanol groups. This step, prior to addition of GUVs, ensured that the pore-rim surface became hydrophilic. Estimation of the contact angles formed by a PBS buffer drop on silanized glass slides modified with three different ethoxysilanes (mercaptopropyl-triethoxysilane (SHTES), aminopropyl-triethoxysilane (APTES), or tetraethoxysilane (TEOS)) showed that the surface was hydrophobic directly after silanization, with a contact angle of about 80° for all three substrates. After 10 s of O_2 plasma treatment, all three surfaces regained their hydrophilic character and the water drop wet the surface with a contact angle <5° (Supporting Information, Figure S6). As we hypothesized that all organic

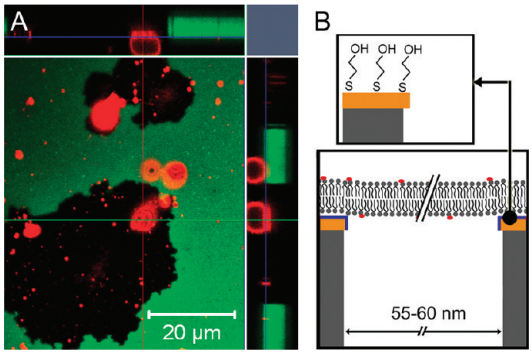

Figure 6. (A) Pore spanning membranes prepared from POPC GUV spreading on AAO functionalized with mercaptoethanol on gold. The membrane excludes Alexa-488 labeled avidin from adsorbing within the AAO nanopores visible as black patches (experimental conditions as in Figure 4). Alexa-488 avidin exclusion was observed but gold quenched the fluorescence of the pore-spanning membrane. (B) Illustration of the pore-rim surface functionalization obtained by evaporation of 2 nm of Cr and 15 nm of Au onto the AAO, followed by a mercaptoethanol self-assembled monolayer.

groups are oxidized by the plasma treatment resulting in a hydrophilic surface, we repeated the selective functionalization procedure of AAO with both TEOS and APTES and found indeed no difference in the spreading behavior of GUVs on the nanoporous substrate. This implies that only the silanol groups remain on the surface and are pivotal for vesicle spreading. In general, we believe that SHTES was a better choice of silane because it produces a lower degree of vertical polymerization.

To further support the idea that a high density of OH-groups on the pore rims is required for the vesicles to spread, we produced an analogous surface functionalization by directly modifying the pore-rim surface of AAO with a mercaptoethanol self-assembled monolayer on gold (Figure 6). We evaporated 2 nm of Cr and 15 nm of Au onto AAO with $d_0 = 60$ nm. Under the same experimental conditions as presented in Figure 4, POPC pore-spanning membrane patches obtained from GUVs, were capable of excluding Alexa-488 avidin, as shown in the confocal *z*-stack image in Figure 6. As gold quenches the fluorescence of the material within a range of about 15 nm, only material that is further than about 20 nm from the gold becomes visible. Thus, the fluorescently labeled pore-spanning membranes cannot be detected by fluorescence imaging. Contrasting Figure 4 and Figure 6 illustrates the advantage of using silane-chemistry *versus* thiol-chemistry on gold to functionalize the AAO pore rims. An evaporated thin gold layer decreases the optical transparency, which decreases the visibility of processes occurring within the AAO, but more importantly, gold does not allow imaging of pore-spanning membrane formation and potential membrane-bound components.[70] To make use of fluorescence enhancement using the gold on the pore-rims, the fluorophores in the bilayer would need

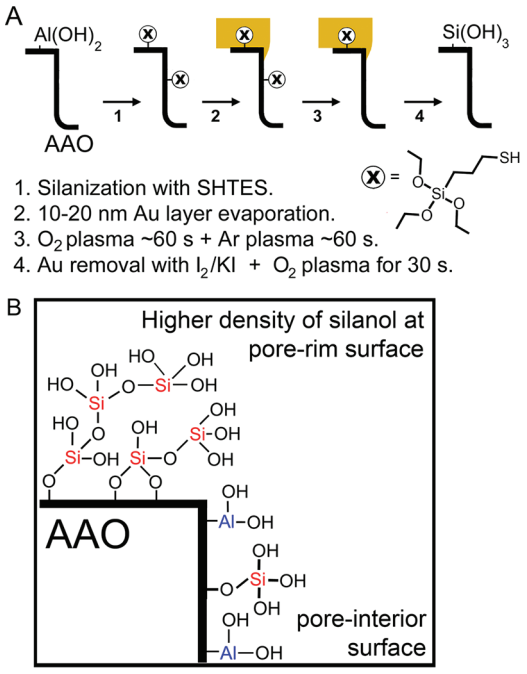

Figure 7. (A) AAO functionalization protocol: (1) AAO is silanized with SHTES, (2) a thin Au layer (protective mask) is evaporated, (3) the pore-interior surface is ablated using both O_2 and Ar plasma and (4) the Au is removed and the pore-rim surface is rendered hydrophilic with a short O_2 plasma treatment. (B) The final AAO substrates have hydrophilic pore rims and most importantly, remain optically transparent.

to be located sufficiently far away from the metal to prevent quenching; at least 15−30 nm from the surface using a deposited dielectric thin-film spacer.[71] In fact, Figure 6 shows fluorescent vesicles on top of the pore-spanning bilayer displaying a slightly enhanced fluorescence, which is probably due to surface-enhanced fluorescence close to the gold surface.

This experiment also shows that differentiating pore-rim and pore-interior surface chemistries can contribute to the formation of stable pore-spanning membranes. We envision that the AAO surface after the silane-based functionalization scheme (Figure 7A) has a surface functionalization as depicted in Figure 7B. The pore-rim surface exhibits a higher density of silanol groups that facilitates the rupture of phospholipid vesicles. Given that the pore-interior surface was exposed to longer periods of plasma treatments, with both O_2 and Ar, the silane functionality was possibly sufficiently ablated that the surface was less active toward lipids. The final substrates therefore behaved similarly to the gold functionalized substrates, but with the invaluable advantage of optical transparency.

CONCLUSIONS

We presented a method that allowed the preparation of fluid laterally mobile pore-spanning membranes on optically transparent nanoporous anodic aluminum oxide (AAO) substrates, with pore diameters of 55−60 nm, by GUV spreading. The method produced stable and solvent-free pore-spanning lipid bilayers separating attoliter-sized compartments. Owing to the optical transparency of the functionalized AAO substrates, the encapsulation of material atop, and more importantly within the porous matrix, could be readily followed by confocal laser scanning fluorescence microscopy. These pore-spanning lipid membranes on AAO isolate the pore-interior chemical environment of several thousand AAO nanopores from the bulk solution. The membrane architecture realizes the desired concept of having two chemically distinct liquid environments isolated by a lipid membrane, which allows the investigation of the transport phenomena driven by (electro)gradients across this membrane. Such gradients can be generated simply by using solutions of different compositions or by transporter proteins. We have shown that the nanoporosity of the AAO allowed us to optically access the interior of the pores. This specifically permits not only fluorescence detection methods but also label-free techniques such as optical waveguide spectroscopy that relies on changes of the dielectric function. As the fluorescence of the lipid bilayers on top of the AAO substrates is not quenched, also the binding/insertion and lateral mobility of peripheral and transmembrane proteins within the lipid bilayer patches can be monitored by fluorescence methods.

MATERIALS AND METHODS

Materials. 1-Palmitoyl-2-oleoyl-*sn*-glycero-3-phosphocholine (POPC) was purchased from Avanti Polar Lipids, Inc. (Alabaster, AL, USA). Lyophilized Alexa-488 labeled avidin (1 mg) and 2-(4,4-difluoro-5-methyl-4-bora-3a,4a-diaza-s-indacene-3-dodecanoyl)-1-hexadecanoyl-*sn*-glycero-3-phosphocholine (Bodipy DHPE) was obtained from Invitrogen (Eugene, OR, USA). Texas Red DHPE was from Biotinum Inc. (Hayward, CA, USA). Oxalic acid dihydrate was purchased from AppliChem (Darmstadt, Germany). $HClO_4$ (70%) and H_3PO_4 (85%) were from Merck (Darmstadt, Germany). Sucrose and pyranine were purchased from Acros Organics (Geel, Belgium). Ethanol was p.a. grade (VWR, Germany). $CuCl_2$ and H_2SO_4 were purchased from Sigma-Aldrich (Germany). Aluminum foils (0.25 mm thick, purity: 99.999%) were purchased from Goodfellow (Huntington, UK). Indium tin oxide (ITO) slides were from Präzisions Glas & Optik GmbH (Iserlohn, Germany). The UV-curable optical adhesive (NOA 83H) was obtained from Norland Products (Cranbury, NJ, USA). Mercaptopropyl-triethoxysilane (SHTES) was purchased from ABCR (Karlsruhe, Germany). Aminopropyl-triethoxysilane (APTES) was from Fluka (Steinheim, Germany), and tetraethoxysilane (TEOS) was from Alfa Aeser (Karlsruhe, Germany). The water used was ion exchanged and filtered using a Millipore system (Milli-Q System from Millipore, Molsheim, France; specific resistance $R > 18\ M\Omega\ cm^{-1}$, pH ≈ 5.5).

Au Evaporation and Removal. Au and Cr were evaporated on a Bal-Tec MCS610 evaporator equipped with a Bal-Tec QSG100 quartz film thickness monitor. For the metal layer at the AAO bottom, 2 nm of Cr and 25 nm of Au were evaporated on the AAO barrier layer. When Au was used as a temporary protective mask for functionalization, only 10−20 nm of Au were evaporated directly onto the AAO pores at a high deposition rate of 1.0 nm s^{-1}.

Plasma Treatments. Argon and oxygen plasma treatments were carried out with a Harrick plasma cleaner (Ithaca, NY, USA), under high power. The vacuum chamber was flushed with the desired gas and evacuated with a rotary vane pump for 2 min. The plasma was turned on and the gas pressure in the chamber was increased to obtain a faint color plasma. Ar (purple) plasma treatments were carried out for 60 s and O_2 plasma (faint blue) treatments were carried out for 60 and 30 s; the duration was calculated using the initiation of the colored plasma as $t = 0$.

Deposition of AAO Membranes on Planar Glass Supports. AAO films anodized from bulk aluminum foil were mounted on microscope glass slides using an optical adhesive according to a previously reported technique.[72] Briefly, AAO thin films were fabricated by electrochemical anodization of aluminum foils, which were annealed at 500 °C overnight. Al foils were electrochemically polished first in a solution of H_2SO_4 (concentrated)/H_3PO_4 (85%)/H_2O (1:1:1) at 25 V. Second, the Al foils were polished in a solution of $HClO_4$/ethanol (1:4, v/v) for 15 min, 0 °C at 20 V. They were then anodized for 2 h in 0.3 M oxalic acid, 1 °C at 40 V. The alumina was removed with a 5 vol % H_3PO_4 solution for 2−3 h. Al foils were then anodized a second time for 1.5 h (3.5 μm thick AAO) or for 3 h (7 μm thick AAO). Al was removed from the anodized Al foil by immersion in 17 g/L $CuCl_2$ in 18.5 M HCl until the AAO became visible and no metal remained. Prior to Al removal, the AAO side was isolated from solution by immobilization onto a glass slide and sealed using epoxy adhesive. Two nm of Cr and 25 nm of Au were evaporated onto the barrier layer of the AAO membranes. The metal does not enter the pores and lies under the AAO barrier layer. It serves as a useful positioning tool to locate the transparent alumina using the microscope. Norland 83H adhesive was diluted in THF (1:10) and spin-coated on LASFN9 glass slides at 20 rpm for 2−3 s. The Au-coated AAO was glued, barrier side down, onto the glue covered glass side and UV-cured for 2 h with a UV hand lamp (Herolab, Wiesloch, Germany), with both lamps on (λ = 254 nm and λ = 354 nm, 4 W). The pore diameter (d_0) for all AAO membranes was widened to the desired diameter by etching in 5 vol % H_3PO_4.

AAO Silanization, Selective Functionalization. AAO substrates were O_2 plasma cleaned for 60 s immediately prior to gas-phase silanization to increase the surface density of OH-groups. The glass slide substrates to be silanized were inserted into a glass staining jar and 50 μL of either SHTES, APTES, or TEOS were added in a glass test tube, inside the chamber. The container was covered with its glass cover and sealed using Scotch vacuum tape (3M, St. Paul, MN, USA), left in the oven at 130 °C for 5 min to warm, followed by 3 h under continuous vacuum. The functionalized samples were cooled. Directly after silanization (step 1), 10−20 nm of Au were evaporated onto the substrates (step 2). They were then treated with O_2 plasma for 60 s, followed by 60 s of Ar plasma (step 3). The substrates could be stored for several weeks in this condition. Before use, the Au layer was removed with I_2/KI solution (50 g/L KI, 12.5 g/L I_2) for 20−30 s. The substrate was then rinsed, dried, O_2 plasma-treated for 30 s (step 4), and used directly.

Fluorescence Microscopy. CLSM measurements were performed with an upright confocal microscope LSM 710 from Carl Zeiss MicroImaging GmbH (Jena, Germany). A 63× water immersion objective (WPlan-APO-CHROMAT, N.A. = 1.0, Zeiss) was used. The *z*-stack images were obtained by acquiring multiple confocal *x*−*y* focal plane images along the vertical *z*-direction, which allow for a three-dimensional image reconstruction. Slices of about 100 nm thick over a 12−20 μm range were acquired with an axial resolution of 0.9 μm.

The upright epi-fluorescence optical microscope BX-51, equipped with a filter for Nile Red (UMNG2), (Olympus Germany GmbH, Hamburg, Germany) was used for video microscopy. A 40× water immersion objective was used (LUMPlanF1 40XW, N.A. = 0.8, Olympus).

Giant Unilamellar Vesicles (GUVs). GUVs were prepared by electroformation.[73] Briefly, 50 μL of a 1 mg/mL POPC solution in chloroform (1 mol % Texas Red DHPE) was dried uniformly on ITO slides. The slides were left at 64 °C under vacuum for at least 3 h. A chamber was assembled using conductive copper tape at the ITO slide edges and a 1 mm thick square Teflon spacer between them (volume: 1.7 mL) and subsequently filled with 0.3 M sucrose solution through an opening. The electroformation cycle was carried out at 12 Hz with voltage increments every 60 s for 3 h: starting at 0.05 V, followed by 0.01 V steps until 0.2 V, finally 0.1 V steps until a constant 1.6 V was applied for the remaining duration. Afterward, a 5 Hz square wave was applied for 10 min. The osmolarity of the sucrose solution was 0.25−0.30 Osm/L and was measured with a cryoscopic osmometer (Osmomat 030, Gonotec, Berlin, Germany). GUVs were stored at 4 °C and used for no longer than 2 weeks. The AAO was rinsed with ethanol, and then the measuring chamber was rinsed and filled with 1.5 mL of PBS buffer (20 mM NaH_2PO_4/Na_2HPO_4, 100 mM NaCl, pH 7.2) before adding the GUVs. The heavier sucrose-filled vesicles sink to the substrate.

For FRAP experiments, 50 μL of GUV suspension was slowly added to the substrate, incubated for 1 h, and rinsed with PBS buffer. FRAP experiments were performed with the CLSM setup on circular regions of interest using POPC membranes doped with 0.1 mol % Bodipy DHPE. For the Alexa-488 avidin exclusion experiments, Texas Red DHPE labeled GUVs were added to the PBS buffer-filled measuring chamber and left to incubate for 30 min. The chamber was rinsed and fluorescently labeled Alexa-488 avidin (0.25 mg/mL) was added, incubated for 1 h, and gently rinsed with buffer. *Z*-stacks were acquired with 1.0 au setting (1.4 μm pinhole), which reduced the fluorescence signal, but increased spatial resolution.

For the molecular encapsulation experiments, 10 mM pyranine in PBS buffer was used. 50 μL GUV suspension was added and incubated for 1 h. After the GUVs were spread, the solution was rinsed extensively to remove the excess of pyranine dye, until the background fluorescence disappeared.

Acknowledgment. A.J. and C.S. gratefully acknowledge financial support from the DFG (JA 963/8, STE 884/9-1 SFB 803). T.D.L. acknowledges the award of a doctoral scholarship from *the Fonds Québécois de Recherche sur la Nature et les Technologies* (FQRNT) and additional financial support from the Göttingen Graduate School for Neurosciences and Molecular Biosciences (GGNB). M.K. acknowledges financial support from MPIP-IMPRS Mainz and IMPRS-PBCS Göttingen for doctoral scholarships.

Supporting Information Available: Figure S1: Behavior of GUVs with different functionalized substrates. Figure S2: Alexa-488 labeled avidin adsorbed on a nonfunctionalized AAO was bleached. Figure S3: High resolution *z*-line profile after bleaching of entrapped pyranine in AAO pores. Figure S4: Fluorescence image of a functionalized AAO after addition of a large GUV concentration. Figure S5: Example of high surface area membrane coverage of AAO, shown with pyranine entrapment. Figure S6: Measurement of contact angle, before and after O_2 treatment of gas-phase silanized glass slides with SHTES, APTES, and TEOS. Movie S1: Vesicle approach and rupture. This material is available free of charge *via* the Internet at http://pubs.acs.org.

REFERENCES AND NOTES

1. Castellana, E. T.; Cremer, P. S. Solid Supported Lipid Bilayers: From Biophysical Studies to Sensor Design. *Surf. Sci. Rep.* **2006**, *61*, 429–444.
2. Richter, R. P.; Berat, R.; Brisson, A. R. Formation of Solid-Supported Lipid Bilayers: An Integrated View. *Langmuir* **2006**, *22*, 3497–3505.
3. Sackmann, E. Supported Membranes: Scientific and Practical Applications. *Science* **1996**, *271*, 43–48.
4. Hubbard, J. B.; Silin, V.; Plant, A. L. Self-Assembly Driven by Hydrophobic Interactions at Alkanethiol Monolayers:

Mechanism of Formation of Hybrid Bilayer Membranes. *Biophys. Chem.* **1998**, *75*, 163–176.
5. Plant, A. L. Supported Hybrid Bilayer Membranes as Rugged Cell Membrane Mimics. *Langmuir* **1999**, *15*, 5128–5135.
6. Sackmann, E.; Tanaka, M. Supported Membranes on Soft Polymer Cushions: Fabrication, Characterization and Applications. *Trends Biotechnol.* **2000**, *18*, 58–64.
7. Tanaka, M.; Sackmann, E. Polymer-Supported Membranes as Models of the Cell Surface. *Nature* **2005**, *437*, 656–663.
8. McBee, T. W.; Wang, L. Y.; Ge, C. H.; Beam, B. M.; Moore, A. L.; Gust, D.; Moore, T. A.; Armstrong, N. R.; Saavedra, S. S. Characterization of Proton Transport Across a Waveguide-Supported Lipid Bilayer. *J. Am. Chem. Soc.* **2006**, *128*, 2184–2185.
9. Naumann, R.; Schiller, S. M.; Giess, F.; Grohe, B.; Hartman, K. B.; Karcher, I.; Köper, I.; Lubben, J.; Vasilev, K.; Knoll, W. Tethered Lipid Bilayers on Ultraflat Gold Surfaces. *Langmuir* **2003**, *19*, 5435–5443.
10. Erbe, A.; Bushby, R. J.; Evans, S. D.; Jeuken, L. J. C. Tethered Bilayer Lipid Membranes Studied by Simultaneous Attenuated Total Reflectance Infrared Spectroscopy and Electrochemical Impedance Spectroscopy. *J. Phys. Chem. B* **2007**, *111*, 3515–3524.
11. Anderson, T. H.; Min, Y. J.; Weirich, K. L.; Zeng, H. B.; Fygenson, D.; Israelachvili, J. N. Formation of Supported Bilayers on Silica Substrates. *Langmuir* **2009**, *25*, 6997–7005.
12. Cremer, P. S.; Boxer, S. G. Formation and Spreading of Lipid Bilayers on Planar Glass Supports. *J. Phys. Chem. B* **1999**, *103*, 2554–2559.
13. Hamai, C.; Cremer, P. S.; Musser, S. M. Single Giant Vesicle Rupture Events Reveal Multiple Mechanisms of Glass-Supported Bilayer Formation. *Biophys. J.* **2007**, *92*, 1988–1999.
14. Rädler, J.; Strey, H.; Sackmann, E. Phenomenology and Kinetics of Lipid Bilayer Spreading on Hydrophilic Surfaces. *Langmuir* **1995**, *11*, 4539–4548.
15. Khan, T. R.; Grandin, H. M.; Mashaghi, A.; Textor, M.; Reimhult, E.; Reviakine, I. Lipid Redistribution in Phosphatidylserine-Containing Vesicles Adsorbing on Titania. *Biointerphases* **2008**, *3*, FA90–FA95.
16. Lagerholm, B. C.; Starr, T. E.; Volovyk, Z. N.; Thompson, N. L. Rebinding of IgE Fabs at Haptenated Planar Membranes: Measurement by Total Internal Reflection with Fluorescence Photobleaching Recovery. *Biochem.* **2000**, *39*, 2042–2051.
17. Tamm, L. K.; McConnell, H. M. Supported Phospholipid-Bilayers. *Biophys. J.* **1985**, *47*, 105–113.
18. Reimhult, E.; Höök, F.; Kasemo, B. Vesicle Adsorption on SiO_2 and TiO_2: Dependence on Vesicle Size. *J. Chem. Phys.* **2002**, *117*, 7401–7404.
19. Savarala, S.; Ahmed, S.; Ilies, M. A.; Wunder, S. L. Formation and Colloidal Stability of DMPC Supported Lipid Bilayers on SiO_2 Nanobeads. *Langmuir* **2010**, *26*, 12081–12088.
20. Claesson, M.; Cho, N. J.; Frank, C. W.; Andersson, M. Vesicle Adsorption on Mesoporous Silica and Titania. *Langmuir* **2010**, *26*, 16630–16633.
21. Lenz, P.; Ajo-Franklin, C. M.; Boxer, S. G. Patterned Supported Lipid Bilayers and Monolayers on Poly(dimethylsiloxane). *Langmuir* **2004**, *20*, 11092–11099.
22. Shahal, T.; Melzak, K. A.; Lowe, C. R.; Gizeli, E. Poly-(dimethylsiloxane)-Coated Sensor Devices for the Formation of Supported Lipid Bilayers and the Subsequent Study of Membrane Interactions. *Langmuir* **2008**, *24*, 11268–11275.
23. Williams, L. M.; Evans, S. D.; Flynn, T. M.; Marsh, A.; Knowles, P. F.; Bushby, R. J.; Boden, N. Kinetics of the Unrolling of Small Unilamellar Phospholipid Vesicles onto Self-Assembled Monolayers. *Langmuir* **1997**, *13*, 751–757.
24. Pera, I.; Stark, R.; Kappl, M.; Butt, H. J.; Benfenati, F. Using the Atomic Force Microscope to Study the Interaction Between Two Solid Supported Lipid Bilayers and the Influence of Synapsin I. *Biophys. J.* **2004**, *87*, 2446–2455.
25. Cha, T.; Guo, A.; Zhu, X. Y. Formation of Supported Phospholipid Bilayers on Molecular Surfaces: Role of Surface Charge Density and Electrostatic Interaction. *Biophys. J.* **2006**, *90*, 1270–1274.
26. Steinem, C.; Janshoff, A.; Ulrich, W. P.; Sieber, M.; Galla, H. J. Impedance Analysis of Supported Lipid Bilayer Membranes: A Scrutiny of Different Preparation Techniques. *Biochim. Biophys. Acta, Biomembr.* **1996**, *1279*, 169–180.
27. Janshoff, A.; Steinem, C. Transport Across Artificial Membranes—An Analytical Perspective. *Anal. Bioanal.Chem.* **2006**, *385*, 433–451.
28. Gassmann, O.; Kreir, M.; Ambrosi, C.; Pranskevich, J.; Oshima, A.; Roling, C.; Sosinsky, G.; Fertig, N.; Steinem, C. The M34A Mutant of Connexin26 Reveals Active Conductance States in Pore-Suspending Membranes. *J. Struct. Biol.* **2009**, *168*, 168–176.
29. Kleefen, A.; Pedone, D.; Grunwald, C.; Wei, R.; Firnkes, M.; Abstreiter, G.; Rant, U.; Tampé, R. Multiplexed Parallel Single Transport Recordings on Nanopore Arrays. *Nano Lett.* **2010**, *10*, 5080–5087.
30. Schmitt, E. K.; Nurnabi, M.; Bushby, R. J.; Steinem, C. Electrically Insulating Pore-Suspending Membranes on Highly Ordered Porous Alumina Obtained from Vesicle Spreading. *Soft Matter* **2008**, *4*, 250–253.
31. Hennesthal, C.; Steinem, C. Pore-Spanning Lipid Bilayers Visualized by Scanning Force Microscopy. *J. Am. Chem. Soc.* **2000**, *122*, 8085–8086.
32. Im, H.; Wittenberg, N. J.; Lesuffleur, A.; Lindquist, N. C.; Oh, S. H. Membrane Protein Biosensing with Plasmonic Nanopore Arrays and Pore-Spanning Lipid Membranes. *Chem. Sci.* **2010**, *1*, 688–696.
33. Kresak, S.; Hianik, T.; Naumann, R. L. C. Gigaseal Solvent-Free Bilayer Lipid Membranes: From Single Nanopores to Nanopore Arrays. *Soft Matter* **2009**, *5*, 4021–4032.
34. Sugihara, K.; Voros, J.; Zambelli, T. A Gigaseal Obtained with a Self-Assembled Long-Lifetime Lipid Bilayer on a Single Polyelectrolyte Multilayer-Filled Nanopore. *ACS Nano* **2010**, *4*, 5047–5054.
35. Mager, M. D.; Melosh, N. A. Nanopore-Spanning Lipid Bilayers for Controlled Chemical Release. *Adv. Mater.* **2008**, *20*, 4423–4427.
36. Mager, M. D.; Almquist, B.; Melosh, N. A. Formation and Characterization of Fluid Lipid Bilayers on Alumina. *Langmuir* **2008**, *24*, 12734–12737.
37. Mager, M. D.; Melosh, N. A. Lipid Bilayer Deposition and Patterning *via* Air Bubble Collapse. *Langmuir* **2007**, *23*, 9369–9377.
38. Schmitt, E. K.; Vrouenraets, M.; Steinem, C. Channel Activity of OmpF Monitored in Nano-BLMs. *Biophys. J.* **2006**, *91*, 2163–2171.
39. Weiskopf, D.; Schmitt, E. K.; Klühr, M. H.; Dertinger, S. K.; Steinem, C. Micro-BLMs on Highly Ordered Porous Silicon Substrates: Rupture Process and Lateral Mobility. *Langmuir* **2007**, *23*, 9134–9139.
40. Han, X. J.; Studer, A.; Sehr, H.; Geissbuhler, I.; Di Berardino, M.; Winkler, F. K.; Tiefenauer, L. X. Nanopore Arrays for Stable and Functional Free-Standing Lipid Bilayers. *Adv. Mater.* **2007**, *19*, 4466–4470.
41. Mey, I.; Stephan, M.; Schmitt, E. K.; Müller, M. M.; Ben Amar, M.; Steinem, C.; Janshoff, A. Local Membrane Mechanics of Pore-Spanning Bilayers. *J. Am. Chem. Soc.* **2009**, *131*, 7031–7039.
42. Jonsson, P.; Jonsson, M. P.; Höök, F. Sealing of Submicrometer Wells by a Shear-Driven Lipid Bilayer. *Nano Lett.* **2010**, *10*, 1900–1906.
43. Worsfold, O.; Voelcker, N. H.; Nishiya, T. Biosensing Using Lipid Bilayers Suspended on Porous Silicon. *Langmuir* **2006**, *22*, 7078–7083.
44. Cunin, F.; Milhiet, P. E.; Anglin, E.; Sailor, M. J.; Espenel, C.; Le Grimellec, C.; Brunel, D.; Devoisselle, J. M. Continuous Planar Phospholipid Bilayer Supported on Porous Silicon Thin Film Reflector. *Ultramicroscopy* **2007**, *107*, 1048–1052.
45. Bhattacharya, J.; Kisner, A.; Offenhäusser, A.; Wolfrum, B. Microfluidic Anodization of Aluminum Films for the Fabrication of Nanoporous Lipid Bilayer Support Structures. *Beilstein J. Nanotechnol.* **2011**, *2*, 104–109.
46. Suzuki, K.; Masuhara, H. Groove-Spanning Behavior of Lipid Membranes on Microfabricated Silicon Substrates. *Langmuir* **2005**, *21*, 6487–6494.

47. Pfeiffer, I.; Seantier, B.; Petronis, S.; Sutherland, D.; Kasemo, B.; Zach, M. Influence of Nanotopography on Phospholipid Bilayer Formation on Silicon Dioxide. *J. Phys. Chem. B* **2008**, *112*, 5175–5181.
48. Pfeiffer, I.; Petronis, S.; Köper, I.; Kasemo, B.; Zach, M. Vesicle Adsorption and Phospholipid Bilayer Formation on Topographically and Chemically Nanostructured Surfaces. *J. Phys. Chem. B* **2010**, *114*, 4623–4631.
49. Simon, A.; Girard-Egrot, A.; Sauter, F.; Pudda, C.; D'Hahan, N. P.; Blum, L.; Chatelain, F.; Fuchs, A. Formation and Stability of a Suspended Biomimetic Lipid Bilayer on Silicon Submicrometer-Sized Pores. *J. Colloid Interface Sci.* **2007**, *308*, 337–343.
50. Knoll, W. Interfaces and Thin Films As Seen by Bound Electromagnetic Waves. *Annu. Rev. Phys. Chem.* **1998**, *49*, 569–638.
51. Lau, K. H. A.; Tan, L. S.; Tamada, K.; Sander, M. S.; Knoll, W. Highly Sensitive Detection of Processes Occurring Inside Nanoporous Anodic Alumina Templates: A Waveguide Optical Study. *J. Phys. Chem. B* **2004**, *108*, 10812–10818.
52. Lazzara, T. D.; Lau, K. H. A.; Abou-Kandil, A. I.; Caminade, A. M.; Majoral, J. P.; Knoll, W. Polyelectrolyte Layer-by-Layer Deposition in Cylindrical Nanopores. *ACS Nano* **2010**, *4*, 3909–3920.
53. Dai, J. H.; Baker, G. L.; Bruening, M. L. Use of Porous Membranes Modified with Polyelectrolyte Multilayers as Substrates for Protein Arrays with Low Nonspecific Adsorption. *Anal. Chem.* **2006**, *78*, 135–140.
54. Takmakov, P.; Vlassiouk, I.; Smirnov, S. Application of Anodized Aluminum in Fluorescence Detection of Biological Species. *Anal. Bioanal. Chem.* **2006**, *385*, 954–958.
55. Casanova, F.; Chiang, C. E.; Li, C. P.; Roshchin, I. V.; Ruminski, A. M.; Sailor, M. J.; Schuller, I. K. Gas Adsorption and Capillary Condensation in Nanoporous Alumina Films. *Nanotechnology* **2008**, *19*, 315709.
56. Janshoff, A.; Dancil, K. P. S.; Steinem, C.; Greiner, D. P.; Lin, V. S. Y.; Gurtner, C.; Motesharei, K.; Sailor, M. J.; Ghadiri, M. R. Macroporous p-Type Silicon Fabry-Perot Layers. Fabrication, Characterization, and Applications in Biosensing. *J. Am. Chem. Soc.* **1998**, *120*, 12108–12116.
57. Schwartz, M. P.; Alvarez, S. D.; Sailor, M. J. Porous SiO_2 Interferometric Biosensor for Quantitative Determination of Protein Interactions: Binding of Protein A to Immunoglobulins Derived from Different Species. *Anal. Chem.* **2007**, *79*, 327–334.
58. Vasilev, K.; Knoll, W.; Kreiter, M. Fluorescence Intensities of Chromophores in Front of a Thin Metal Film. *J. Chem. Phys.* **2004**, *120*, 3439–3445.
59. Lau, K. H. A.; Knoll, W.; Kim, D. H. Theoretical Optical Waveguide Investigation of Self-Organized Polymer Thin Film Nanostructures with Nanoparticle Incorporation. *Macromol. Res.* **2007**, *15*, 211–215.
60. Ono, S.; Masuko, N. The Duplex Structure of Cell-Walls of Porous Anodic Films Formed on Aluminum. *Corros. Sci.* **1992**, *33*, 503–505.
61. Lazzara, T. D.; Kliesch, T. T.; Janshoff, A.; Steinem, C. Orthogonal Functionalization of Nanoporous Substrates: Control of 3D Surface Functionality. *ACS Appl. Mater. Interfaces* **2011**, *3*, 1068–1076.
62. Aronsson, B. O.; Lausmaa, J.; Kasemo, B. Glow Discharge Plasma Treatment for Surface Cleaning and Modification of Metallic Biomaterials. *J. Biomed. Mater. Res.* **1997**, *35*, 49–73.
63. Raiber, K.; Terfort, A.; Benndorf, C.; Krings, N.; Strehblow, H. H. Removal of Self-Assembled Monolayers of Alkanethiolates on Gold by Plasma Cleaning. *Surf. Sci.* **2005**, *595*, 56–63.
64. Axelrod, D.; Koppel, D. E.; Schlessinger, J.; Elson, E.; Webb, W. W. Mobility Measurement by Analysis of Fluorescence Photobleaching Recovery Kinetics. *Biophys. J.* **1976**, *16*, 1055–1069.
65. Stelzle, M.; Miehlich, R.; Sackmann, E. 2-Dimensional Microelectrophoresis in Supported Lipid Bilayers. *Biophys. J.* **1992**, *63*, 1346–1354.
66. Przybylo, M.; Sykora, J.; Humpolickova, J.; Benda, A.; Zan, A.; Hof, M. Lipid Diffusion in Giant Unilamellar Vesicles is more than 2 Times Faster than in Supported Phospholipid Bilayers under Identical Conditions. *Langmuir* **2006**, *22*, 9096–9099.
67. Lazzara, T. D.; Mey, I.; Steinem, C.; Janshoff, A. Benefits and Limitations of Porous Substrates as Biosensors for Protein Adsorption. *Anal. Chem.* **2011**, *83*, 5624–5630.
68. Boxer, S. G. Molecular Transport and Organization in Supported Lipid Membranes. *Curr. Opin. Chem. Biol.* **2000**, *4*, 704–709.
69. Nissen, J.; Gritsch, S.; Wiegand, G.; Rädler, J. O. Wetting of Phospholipid Membranes on Hydrophilic Surfaces—Concepts Towards Self-Healing Membranes. *Eur. Phys. J. B* **1999**, *10*, 335–344.
70. Kocun, M.; Lazzara, T. D.; Steinem, C.; Janshoff, A. Preparation of Solvent-Free, Pore-Spanning Lipid Bilayers: Modeling the Low Tension of Plasma Membranes. *Langmuir* **2011**, *27*, 7672–7680.
71. Guo, P. F.; Wu, S.; Ren, Q. J.; Lu, J.; Chen, Z. H.; Xiao, S. J.; Zhu, Y. Y. Fluorescence Enhancement by Surface Plasmon Polaritons on Metallic Nanohole Arrays. *J. Phys. Chem. Lett.* **2010**, *1*, 315–318.
72. Lazzara, T. D.; Lau, K. H. A.; Knoll, W. Mounted Nanoporous Anodic Alumina Thin Films as Planar Optical Waveguides. *J. Nanosci. Nanotechnol.* **2010**, *10*, 4293–4299.
73. Bagatolli, L. A.; Parasassi, T.; Gratton, E. Giant Phospholipid Vesicles: Comparison Among the Whole Lipid Sample Characteristics using Different Preparation Methods—A Two Photon Fluorescence Microscopy Study. *Chem. Phys. Lipids* **2000**, *105*, 135–147.